JACS
JOURNAL OF THE AMERICAN CHEMICAL SOCIETY
pubs.acs.org/JACS
Article

Synthetic Placement of Active Sites in MFI Zeolites for Selective Toluene Methylation to *para*-Xylene

Sopuruchukwu Ezenwa, Hansel Montalvo-Castro, Alexander J. Hoffman, Huston Locht, Jordan Attebery, Deng-Yang Jan, Michael Schmithorst, Bradley Chmelka, David Hibbitts,* and Rajamani Gounder*

Cite This: *J. Am. Chem. Soc.* 2024, 146, 10666−10678

ABSTRACT: Brønsted acidic zeolites are ubiquitous catalysts in fuel and chemical production. Broadening the catalytic diversity of a given zeolite requires strategies to manipulate the acid site placement at framework positions within distinct microporous locations. Here, we combine experiment and theory to elucidate how intermolecular interactions between organic structure-directing agents (OSDAs) and framework Al centers influence the placement of H^+ sites in distinct void environments of MFI zeolites and demonstrate the catalytic consequences of active site location on kinetically controlled (403 K) toluene methylation to xylene regioisomers. Kinetic measurements, interpreted using mechanism-derived rate expressions and transition state theory, alongside density functional theory (DFT) calculations show that larger intersection environments similarly stabilize all three xylene isomer transition states without altering well-established aromatic substitution patterns (*ortho*/*para*/*meta* ∼ 60%:30%:10%), while smaller channel environments preferentially destabilize transition states that form bulkier *ortho*- and *meta*-isomers, thereby resulting in high intrinsic *para*-xylene selectivity (∼80%). DFT calculations reveal that the flexibility of nonconventional OSDAs (e.g., 1,4-diazabicyclo[2.2.2]octane) to reorient within MFI intersections and their ability to hydrogen-bond to form protonated complexes favor the placement of Al in smaller channel environments compared to conventional quaternary OSDAs (e.g., tetra-*n*-propylammonium). These molecular-level insights establish a mechanistic link between OSDA structure, active site placement, and transition state stability in MFI zeolites and provide active site design strategies that are orthogonal to crystallite design approaches harnessing complex reaction-diffusion phenomena to enhance regioisomer selectivity in the industrial production of valuable polymer precursors.

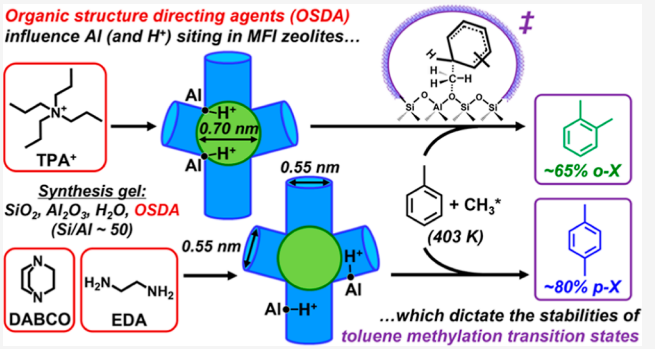

1. INTRODUCTION

Zeolites are crystalline, microporous aluminosilicates that have enabled wide-ranging applications in adsorption, separation, and catalysis[1−3] based on shape selectivity, which describes how micropores regulate molecular access to and from active sites and impose steric constraints that prevent the formation of certain transition states.[4] Zeolites are a family of materials comprising diverse pore shapes, sizes, and interconnectivities, with ∼250 topologies that can be accessed experimentally[5] and >1 million plausible structures identified by theory.[6] Despite such diversity of framework topologies, only ∼10 zeolites have been successfully scaled up and implemented in large-scale commercial applications,[7] motivating research to engineer catalytic diversity in these industrially relevant materials at atomic length scales. One emerging approach is to develop (post)synthetic methods to alter the distribution of aluminum (Al) substituents among tetrahedral-sites (T-sites) in the SiO_2-framework,[8,9] which introduce anionic lattice charges ($[AlO_{4/2}]^-$) that are compensated by Brønsted acid sites (H^+, Figure 1B). This approach is particularly efficacious at broadening catalytic diversity for a given zeolite because transition states are stabilized differently by confinement effects when H^+ sites are positioned within different microporous voids[10] and by intermolecular interactions when multiple H^+ sites are positioned at different relative proximities.[11]

Although the distribution of Al atoms in a given zeolite framework is known to vary with crystallization conditions, its dependence on these conditions is imprecisely understood.[8,9] Theoretical and experimental studies[12−16] have recognized that Al siting is influenced by electrostatic interactions between cationic structure-directing agents (SDAs) and anionic charges at framework $[AlO_{4/2}]^-$ centers.[12] MFI is a low-symmetry

Received: January 9, 2024
Revised: March 21, 2024
Accepted: March 22, 2024
Published: April 4, 2024

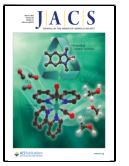

https://doi.org/10.1021/jacs.4c00373
J. Am. Chem. Soc. 2024, 146, 10666−10678

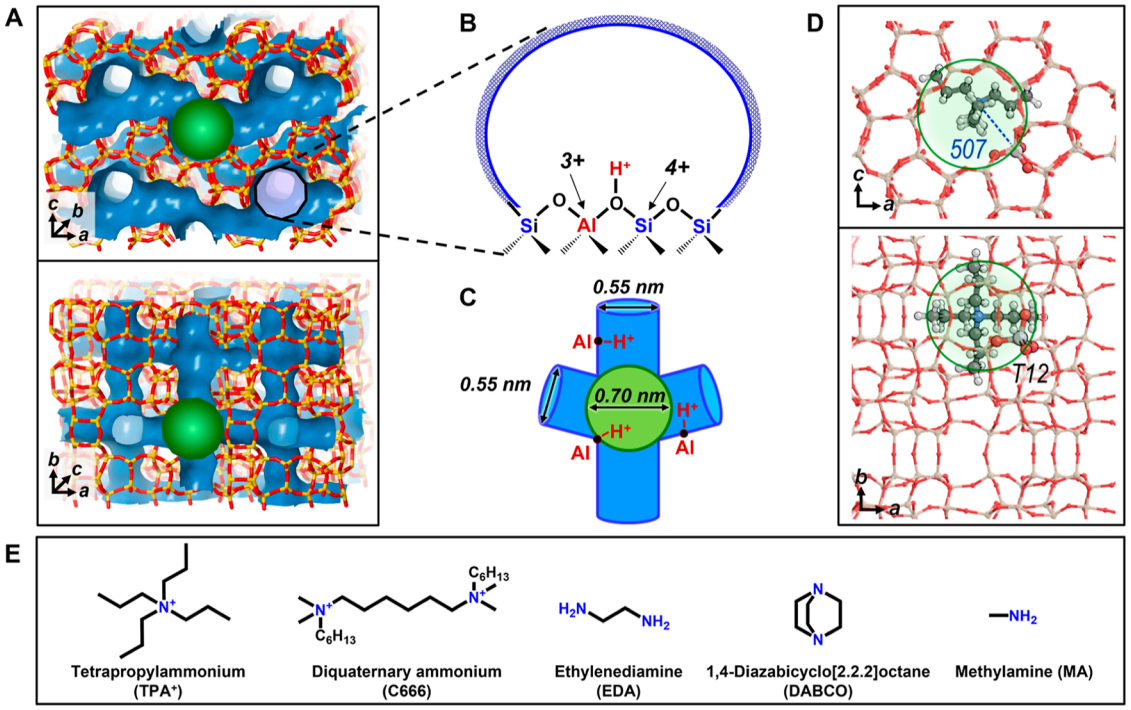

Figure 1. MFI pore and active site structures. (A) MFI topology with sinusoidal and straight channels (blue) and intersections (green).[5] (B) Two-dimensional representation of the proton active site (H^+) that compensates the anionic charge introduced from Si^{4+} substitution by Al^{3+}. (C) Schematic representation of active site locations in different MFI voids. (D) TPA^+ in the intersection of MFI interacting with an anionic Al center (T12 site). (E) OSDAs used to synthesize MFI in this study.

framework (orthorhombic phase) with 12 crystallographic distinct T-sites and 26 distinct oxygen atoms (O_f) located around 10-membered ring (10-MR) straight and sinusoidal channels (~0.55 nm diameter) or channel intersections (~0.70 nm diameter, Figure 1A,C).[5,12] The conventional organic SDA (OSDA) used to crystallize MFI is tetra-*n*-propylammonium (TPA^+), which contains a quaternary N^+ center that is occluded in channel intersections (Figure 1D) and confers energetic preference to position Al in T-sites closest to this N^+ center.[12] This suggests that altering the molecular structure of the SDAs and how they occlude within porous zeolite voids can bias Al siting in the lattice, as has been inferred for MFI synthesized using different organic molecules from changes in heuristic probe reactions (e.g., constraint index) used to assess the local topology around active sites.[17−20] However, a mechanistic link between SDA structure and Al siting and, in turn, transition state stability for MFI, is needed to fully realize the potential of designing SDAs that can place active sites at distinct environments, which stabilize desired transition states and reactive intermediates, and allow synthesizing, *a priori*, zeolites of tailored reactivity.[21−25]

MFI zeolites are used widely in industrial catalytic applications, including aromatic reactions.[1,2] Para-xylene (*p*-X), a valuable polymer precursor, can be obtained alongside its regioisomers (*ortho*-xylene, *o*-X and *meta*-xylene, *m*-X) by upgrading aromatics (e.g., toluene disproportionation and toluene-trimethylbenzene transalkylation),[1,26] among which toluene methylation by dimethyl ether (DME) or methanol (Scheme 1) is a desirable route.[26] Toluene methylation to *p*-X is limited because it is a minor product at thermodynamic equilibrium (~50% *m*-X, ~25% *p*-X, ~25% *o*-X; 573−673 K)[27] and under kinetic control by electrophilic aromatic substitution (~60% *o*-X, ~30% *p*-X, ~10% *m*-X)[28] on acid catalysts.[2]

Scheme 1. Reaction Scheme for Methylation of Toluene with DME or Methanol to Form Xylene[a,b]

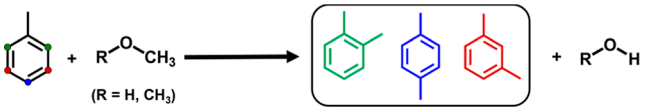

[a]Ring positions for toluene methylation corresponding to each xylene are distinguished: *o*-X (green), *m*-X (red), and *p*-X (blue). [b]R = CH_3 for DME, while R = H for methanol.

However, during typical operating conditions (573−773 K), MFI zeolites can produce *p*-X in higher quantities (30−99%) provided intracrystalline diffusion properties are manipulated to favor sieving of the faster-diffusing *p*-X isomer and by eliminating acid sites at unconfined crystallite surfaces that may catalyze unselective toluene methylation or xylene isomerization reactions.[26,29−32] These conventional design approaches for MFI zeolites require optimizing the interplay between complex reaction networks (Scheme S1, Supporting Information) and transport phenomena to obtain high *p*-X selectivities,[30,31] as they do not alter the intrinsic kinetically controlled product distribution at active sites within intraporous environments. However, active site design strategies that alter intrinsic selectivities should be possible, as proposed for MWW zeolites containing acid sites located within smaller sinusoidal channels that result in higher *p*-X selectivity as acid sites in larger supercages and surface pockets deactivated by coking during toluene methylation at high-temperature and pressure reaction conditions (623 K, 4.2 MPa, 3:1 toluene to methanol).[33]

Here, we use toluene methylation as a catalytic probe reaction (which also happens to be of commercial importance) to establish molecular-level synthesis−structure−function

https://doi.org/10.1021/jacs.4c00373
J. Am. Chem. Soc. 2024, 146, 10666−10678

Table 1. Characterization Data of MFI Zeolites Synthesized Using Varying Structure Directing Agents[h]

sample[a]	synthesis SDAs[b]	Si/Al$_{tot}$[c]	Al per unit cell[d]	H$^+$/Al$_{tot}$[e]	Al^{IV}/total NMR visible Al[f]	micropore volume[g] /cm^3 g^{-1}	crystallite size[h] /μm
MFI-TPA-C	presumably TPA$^+$	43	2.2	0.85	0.98	0.15	1.0 ± 0.7
MFI-TPA-1	TPA$^+$	50	1.9	1.01	0.96	0.17	0.56 ± 0.14
MFI-TPA-2	TPA$^+$	59	1.6	0.84	0.97	0.16	0.61 ± 0.16
MFI-TPA-3	TPA$^+$, Na$^+$	55	1.7	0.97	0.96	0.15	3.3 ± 0.7
MFI-TPA-4	TPA	42	2.2	0.81		0.16	0.35 ± 0.13
MFI-TPA-C666	C666, Na$^+$	47	1.9	0.81	0.97	0.17	0.10 ± 0.04
MFI-EDA-1	EDA, TPA$^+$	53	1.7	1.02	0.99	0.13	1.0 ± 0.5
MFI-EDA-2	EDA, TPA$^+$	58	1.6	0.92	0.97	0.12	8.2 ± 1.6
MFI-EDA-3	EDA, TPA$^+$	49	2.0	0.70	0.97	0.12	0.61 ± 0.61
MFI-EDA-4	EDA, TPA$^+$	55	1.7	0.77		0.15	0.43 ± 0.15
MFI-DABCO-1	DABCO, MA, Na$^+$	44	2.1	0.95	0.98	0.14	12.7 ± 2.1
MFI-DABCO-2	DABCO, MA, Na$^+$	44	2.1	0.87	0.98	0.14	3.3 ± 0.6

[a]Sample nomenclature is MFI-*X*−*Y*, where *X* indicates the major organic SDA and *Y* denotes each unique synthesis, as discussed in Section S1 (Supporting Information). MFI-TPA-C666 was synthesized using a TPA$^+$-like diquaternary OSDA (C666). [b]SDAs used during synthesis. SDA compositions in the synthesis gel are found in Section S1 (Supporting Information), while those in the as-synthesized solids are summarized in Table S9 (Supporting Information). [c]Determined from ICP−OES (Si and Al) or AAS (Al). Uncertainties are ±10%. [d]Calculated from elemental analysis and the unit cell formula. [e]Determined from liquid-phase NH_4^+ ion exchange followed by NH_3 TPD. [f]Determined using ^{27}Al SS MAS NMR. Integrated Al^{IV} intensity includes the ^{27}Al NMR signal at 56 ppm and spinning sidebands, as shown in Figure S30 (Supporting Information). Uncertainties are ±0.05. [g]Determined from N_2 adsorption isotherms at 77 K by linear extrapolation of the volumetric uptake of liquid N_2 at 0.05−0.35 P/P_0 to zero pressure. Uncertainties are ±0.01 cm^3 g^{-1}. [h]Average crystallite size determined by SEM. Uncertainties represent one standard deviation.

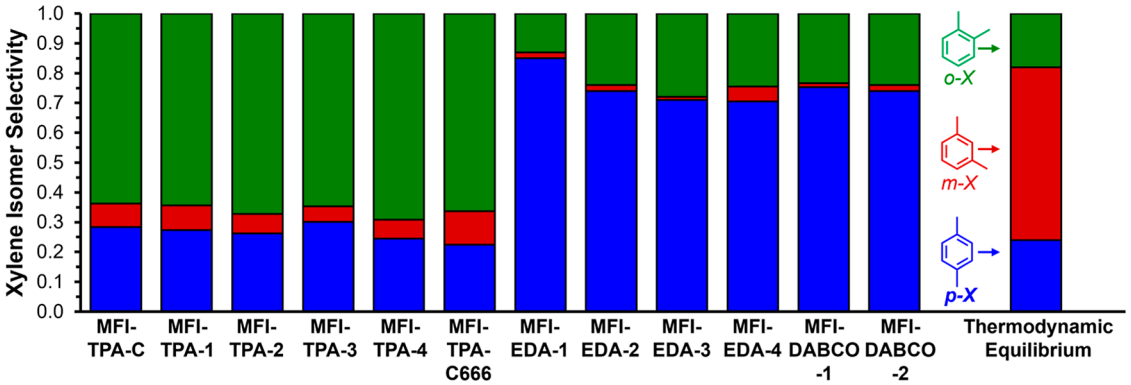

Figure 2. Xylene isomer selectivity during toluene methylation on MFI zeolites (403 K, 4 kPa toluene, 66 kPa DME) and the thermodynamic xylene distribution[27] at 400 K (*p*-X/X = 0.24, *m*-X/X = 0.58, and *o*-X/X = 0.18).

relationships between OSDA structure, active site placement, and transition state stability in MFI zeolites. We investigate toluene methylation at low-temperature conditions (<433 K) that suppress contributions of side reactions (e.g., xylene isomerization and toluene disproportionation) and intracrystalline xylene diffusion restrictions,[29−31,34] to preserve the link between the kinetically relevant transition states that form xylene isomers and the intrazeolite location of acid sites where they form.[35] Experiment and theory combined show that using OSDAs whose structures differ from TPA$^+$ and permit additional intermolecular interactions (e.g., H-bonding) between OSDAs and framework Al during synthesis leads to markedly different distributions of Al among the different void environments within MFI zeolites and, in turn, results in distinct kinetic preferences to form *p*-X by altering transition state stabilities. These findings provide catalyst design strategies orthogonal to those derived using conventional wisdom based on altering intracrystalline diffusion properties to achieve high regioisomer selectivity.

2. RESULTS AND DISCUSSION

2.1. Selectivity and Rates Differ among MFI Zeolites of Different Provenance. We obtained one commercial MFI sample (Zeolyst CBV8014), surmised to be synthesized using TPA$^+$ (MFI-TPA-C), and synthesized various MFI samples (Table 1) with similar composition (Si/Al ≈ 50) using different combinations of organic (Figure 1E) and inorganic (Na^+) SDAs; in some cases, modifications were performed to alter crystallite sizes (synthesis methods and additional characterization data are found in Sections S1 and S2, Figures S32−S45, and Table S9, Supporting Information). We used the conventional TPA$^+$ as the sole OSDA to synthesize samples MFI-TPA-1−4 with mean crystallite sizes of 0.4−3.3 μm and a TPA$^+$-like diquaternary ammonium OSDA (C666) to synthesize a nanosized sample (MFI-TPA-C666) with a mean crystallite size of 0.10 μm (Table 1). We also prepared, using nonconventional OSDAs, MFI-EDA-1−4 using ethylenediamine (EDA) with minor quantities of TPA$^+$ as the co-SDA (EDA/TPA$^+$ = 15) in a "mixed-template" system (additional discussion in Section S5.13, Supporting Information), and MFI-DABCO-1−2 using a mixture of 1,4-

https://doi.org/10.1021/jacs.4c00373
J. Am. Chem. Soc. 2024, 146, 10666−10678

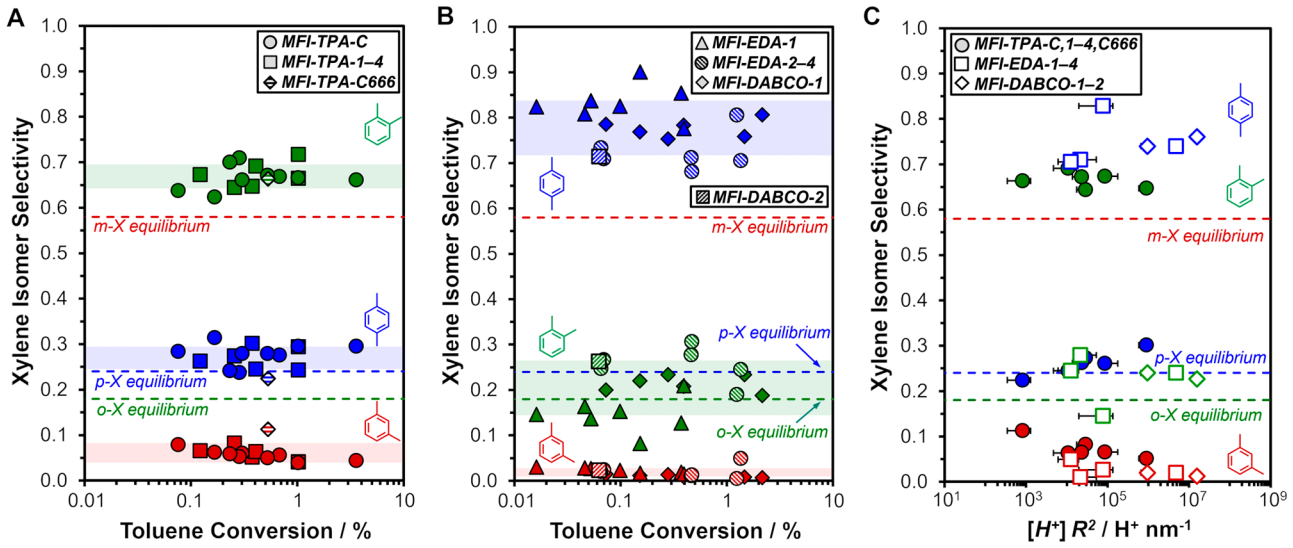

Figure 3. Xylene isomer selectivity during toluene methylation (403 K) on MFI zeolites as a function of (A,B) the toluene conversion (0.016−3.5%) at varying reactant pressures (0.2−8.8 kPa toluene, 25−66 kPa DME) and (C) the product of bulk proton density and square of diffusion path length ($[H^+]$ R^2) at fixed reactant pressures (3.7−4.7 kPa toluene, 66−68 kPa DME). Horizonal shaded region spans the average xylene isomer selectivity plus or minus one standard deviation for (A) MFI-TPA-C, MFI-TPA-1−4, and MFI-TPA-C666 samples and (B) MFI-EDA-1−4 and MFI-DABCO-1,2 samples. Horizontal dashed lines in (A−C) represent the thermodynamic distribution at 400 K (*p*-X/X = 0.24, *m*-X/X = 0.58, and *o*-X/X = 0.18).[27] Error bars on $[H^+]$ R^2 reflect uncertainties propagated from the uncertainties in bulk proton density and the uncertainties in the length of the shortest dimension of the crystallites estimated by SEM.

diazabicyclo[2.2.2]octane (DABCO) and methylamine (MA) as co-SDAs (DABCO/MA = 1), with mean crystallite sizes of 0.4−13 μm (Table 1). All samples had nearly full incorporation of Al into framework positions, as determined by H^+ titration (H^+/Al_{tot} > 0.70; Table 1) and solid-state ^{27}Al nuclear magnetic resonance (NMR) spectroscopy (Al^{IV}/Al_{tot} > 0.95; Table 1).

MFI samples were evaluated for toluene methylation at low temperatures (403 K) and conversions (<2%) to reduce contributions of side reactions and intrazeolite diffusion constraints,[29,31,36,37] conditions distinct from most literature reports (573−773 K, >10% conversion).[26] Using DME as the methylating agent at high DME/toluene ratios (>8:1) drives the reaction network toward toluene−DME methylation and away from toluene disproportionation,[37] yet promotes further methylation to C_{9+} polymethylbenzenes (<3% of gas-phase aromatic products) that slowly accumulate within micropores and cause deactivation. Thus, rates and selectivities are extrapolated to zero time-on-stream and reported as initial values (details in Section S5.2, Supporting Information).

Product distributions on MFI-TPA-1−4 (and -C666) were similar to the commercial MFI sample (MFI-TPA-C), with *o*-X as the major product (64−66% of xylenes) and *p*-X in about half that amount (22−30%) (Figure 2 and Table S3, Supporting Information). Remarkably, the other six MFI samples synthesized using nonconventional SDAs (MFI-EDA-1−4 and MFI-DABCO-1,2) formed *p*-X as the major product (71−85%) with *o*-X as a minor product (13−28%). For all samples, *m*-X was a minor product (1−11%) formed in subequilibrium amounts (Figure 2).[27] *p*-X/*o*-X ratios (0.4−0.5) on conventional MFI samples are similar to previous reports of toluene methylation (288−523 K, 0.7−6.0% toluene conversion) on MFI synthesized using TPA^+,[29] on unconfined acids including homogeneous Friedel−Crafts catalysts ($AlCl_3$, $AlBr_3$, and $BF_3{\cdot}P_2O_5$),[38,39] and on amorphous silica−alumina[40] (Section S5.5 and Table S2, Supporting Information). This selectivity pattern (~65% *o*-X, ~27% *p*-X, and ~8% *m*-X) reflects the relative stabilities of xylenium cations, which favor *o*-X and *p*-X over *m*-X due to resonance and inductive effects[2,28] and symmetry differences in toluene that favor *o*-X and *m*-X over *p*-X. These xylenium cation stability trends and their influences on toluene methylation barriers were confirmed here with gas-phase density functional theory (DFT) calculations (details in Sections S4 and S5.14, Supporting Information). The isomer selectivity (*p*-X/*o*-X = 3−7) on MFI-EDA and MFI-DABCO samples deviate markedly from expected aromatic substitution patterns, as observed on MFI-TPA and unconfined acids, and must reflect phenomena that cannot be solely explained by resonance and inductive effects.

We evaluated and discarded the possibility that measured rates and selectivities were influenced by extracrystalline (packed bed) or intracrystalline residence times, as both are reported to significantly affect xylene selectivity at higher temperatures (>573 K).[26,29−31] Xylene formation rates (403 K, 4 kPa toluene, 67 kPa DME, <0.5% toluene conversion) on three representative MFI samples (MFI-TPA-C, MFI-EDA-1, and MFI-DABCO-1) were invariant with bed residence time (Figure S9, Supporting Information), demonstrating differential reactor operation unaffected by extracrystalline bed-scale transport phenomena (additional discussion in Section S5.3, Supporting Information). Xylene isomer selectivities (403 K, 0.2−8.8 kPa toluene, 25−66 kPa DME) within either the MFI-TPA subset or the MFI-EDA/-DABCO subset were invariant with toluene conversion (0.02−3.5%; Figure 3A,B) and persisted at higher conversions (up to 15% for MFI-TPA-C) despite increased formation of more highly substituted aromatics (up to 5 mol % C_{9+}) (Section S5.3 and Figure S10, Supporting Information), indicating that secondary xylene isomerization reactions across the reactor bed-length are negligible. Further, rates and selectivity were independent of intracrystalline residence times, which depend on the H^+

https://doi.org/10.1021/jacs.4c00373
J. Am. Chem. Soc. 2024, 146, 10666−10678

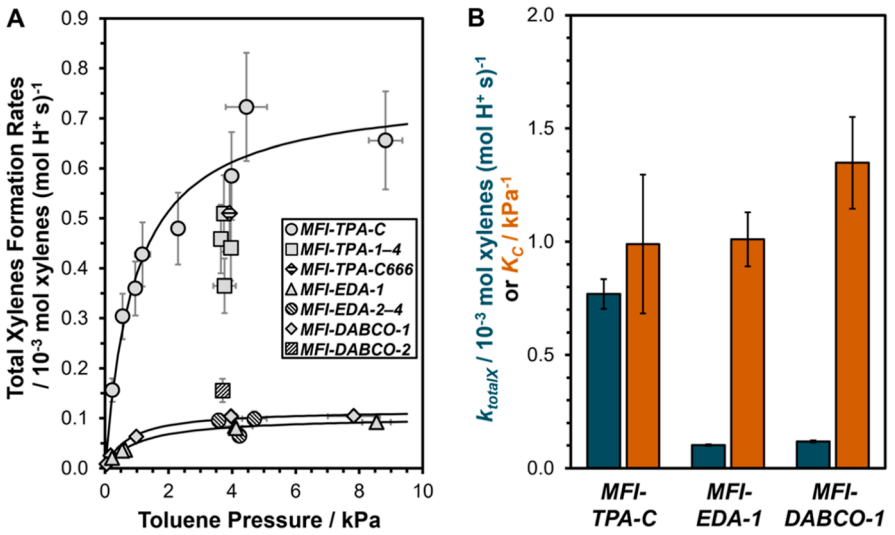

Figure 4. (A) Xylene formation rates as a function of toluene pressure (0.05−8.8 kPa) on representative MFI zeolite samples (MFI-TPA-C, MFI-EDA-1, and MFI-DABCO-1) during toluene methylation (403 K, 66 kPa DME), where solid lines represent regressed best fits to eq 3. Xylene formation rates were obtained for the rest of the MFI samples at a fixed toluene pressure (4.0 ± 0.3 kPa of toluene). Error bars for xylene formation rates represent ±15% uncertainty in rate measurements; error bars for toluene pressure represent one standard deviation of the average toluene pressure. (B) Regressed rate parameters k_{totalX} (obtained from sum of k_{iX}) and K_C for representative MFI zeolite samples (MFI-TPA-C, MFI-EDA-1, and MFI-DABCO-1) with error bars representing two times the standard error of the nonlinear regression fits (details in Section S5.7, Supporting Information).

density (per crystallite volume), the effective diffusion path length (estimated from crystallite sizes), and effective molecular diffusivities. H^+ densities are similar among the MFI samples studied (Table 1), and effective diffusivities should remain constant for a given framework topology (although internal structural defects may influence diffusional barriers[41−43]). Therefore, in a regime controlled by intrazeolite diffusion, increasing the diffusion path length would cause rates to decrease and selectivities to increase to the faster diffusing *p*-X isomer ($D_{p\text{-}X}/D_{m\text{-},o\text{-}X} \approx 10^2$ to 10^3),[30,36] as observed in high-temperature (573−773 K) studies[26,29−31] (additional discussion in Section S5.4, Supporting Information). However, xylene formation rates (Figures S11 and S12, Supporting Information) and isomer selectivities (Figure 3C) were invariant for MFI-TPA (0.10−3.3 μm) and MFI-EDA/-DABCO (0.4−13 μm) samples despite changes in their crystallite sizes by factors of ∼30 (Table 1 and Figures S34−S45, Supporting Information), consistent with operation in a kinetically controlled regime. Taken together, these data indicate that observed rate and selectivity differences between the two subsets of MFI samples reflect intrinsic kinetic differences to form xylene isomers, uninfluenced by transport phenomena, a conclusion that will be further supported by theoretical (DFT) data.

Furthermore, because product selectivities on MFI-TPA samples resemble those for unconfined acids[38−40] and because external acid sites are implicated to isomerize xylenes,[26,32] 2,6-di-*tert*-butylpyridine (DTBP) was cofed during toluene methylation to selectively poison acid sites on external crystallite surfaces and resulted in negligible changes (<10%) in initial rates and selectivities (Section S5.9 and Figures S20−S24, Supporting Information), confirming that contributions of internal acid sites predominate. We also evaluated and discarded alternate hypotheses that kinetic data were influenced by the relative proximity of acid sites (Section S5.11 and Figures S27−S28, Supporting Information).

In addition to these selectivity differences, xylene formation rates (per H^+) also differed significantly between MFI synthesized using conventional or nonconventional SDAs (Figure 4A). Rates on MFI-TPA samples were 4−9× higher than those synthesized using either EDA or DABCO, while rates among samples within either group varied within 2×. We performed detailed kinetic experiments on three representative samples (MFI-TPA-C, MFI-EDA-1, and MFI-DABCO-1) to interrogate the mechanistic origins of these differences. On all three samples, toluene methylation rates (per H^+) transitioned from a first-order to a zero-order dependence with increasing toluene pressures (Figure 4A), rates were zero-order in DME pressure (25−66 kPa; Figure S13a, Supporting Information), and selectivities were invariant with toluene pressures (0.05−8.8 kPa; Figures S14c and S15c, Supporting Information) and DME pressures (25−66 kPa; Figure S13b, Supporting Information). Using methanol (1−4 kPa) instead of DME as the methylating agent weakly influences the observed selectivity (Table S3, Supporting Information). These kinetic trends are consistent with parallel reaction steps that form each xylene isomer from the same reactive intermediate.

A sequence of elementary steps for toluene methylation with DME via the sequential (or dissociative or indirect) mechanism (depicted in Scheme 2) was proposed based on these observations and insights from prior work.[37,44,45] The reaction sequence begins with the quasi-equilibrated (QE) adsorption of DME from the gas phase ($(CH_3)_2O_{(g)}$) onto a Brønsted acid site (H−Z) (step 1; Scheme 2) and subsequent QE methylation of the zeolite to form a surface methoxy species (CH_3−Z) while liberating methanol into the gas phase ($CH_3OH_{(g)}$) (step 2; Scheme 2). This latter step is followed by the QE coadsorption of toluene from the gas phase ($C_7H_{8(g)}$) onto CH_3−Z (step 3; Scheme 2) and then the irreversible and kinetically relevant C−C bond formation between coadsorbed toluene-surface methoxy intermediates (C_7H_8−CH_3−Z) to form xylenes that desorb into the gas phase ($C_8H_{10(g)}$) (step 4; Scheme 2).

https://doi.org/10.1021/jacs.4c00373
J. Am. Chem. Soc. 2024, 146, 10666−10678

Scheme 2. Proposed Sequence of Elementary Steps (via Sequential Mechanism) for the Methylation of Toluene with DME on a Brønsted Acid Zeolite[a]

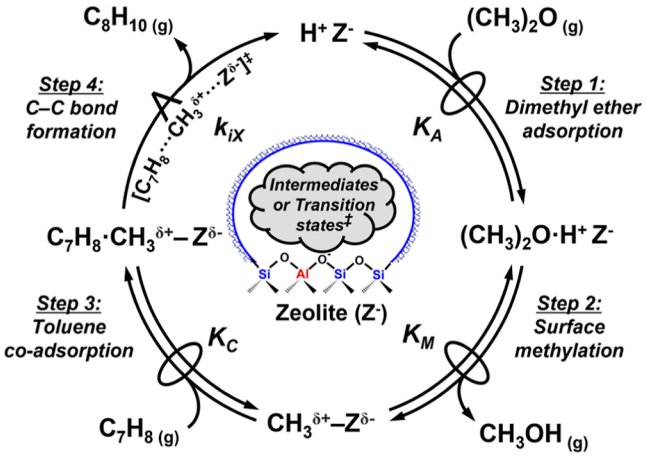

[a]The symbol ⇌ represents a QE step, while the symbol → represents the kinetically relevant step.

Based on the sequence of elementary steps, the full rate expression (eq 1) for the xylene formation rates (r_{iX}) per total number of acid sites ($[L]$) accessible to reactants regardless of their state (unoccupied or occupied by guest species) can be derived in terms of the partial pressures of gas-phase reactants and products (P_{DME}, P_{MeOH}, and $P_{Toluene}$), equilibrium constants, and rate constants (full derivation and additional discussions in Section S5.7, Supporting Information)

$$\frac{r_{iX}}{[L]} = \frac{k_{iX}K_C K_M K_A \frac{P_{DME}}{P_{MeOH}} P_{Toluene}}{1 + K_A P_{DME} + K_M K_A \frac{P_{DME}}{P_{MeOH}} + K_C K_M K_A \frac{P_{DME}}{P_{MeOH}} P_{Toluene}} \quad (1)$$

where K_A, K_M, and K_C are, respectively, the equilibrium constants for DME adsorption, surface methylation, and toluene-C_1 coadsorption, while k_{iX} represents the forward rate constant for C–C bond formation to form xylene isomer *i*. The denominator terms, in order, respectively, represent ratios (relative to H–Z) of concentrations of unoccupied Brønsted acid sites (H–Z), adsorbed DME ($(CH_3)_2O$·H–Z), surface methoxides (CH_3–Z), and coadsorbed toluene-surface methoxides (C_7H_8–CH_3–Z). At the high DME/toluene ratios ($P_{DME}/P_{Toluene} > 8$) in the reactor influent and the high DME/methanol pressures measured in the reactor effluent ($P_{DME}/P_{MeOH} > 1000$), surface methoxides and toluene coadsorbed with surface methoxides are assumed to be the most abundant surface intermediates (MASI) under the study conditions (403 K, >25 kPa DME). This assumption further stems from insights from previous experimental studies (discussed in Section S5.7, Supporting Information) during toluene methylation with DME (29–68 kPa DME, 353–403 K)[37] and CO methylation with DME (1–67 kPa DME, 423–463 K)[45,46] that provided kinetic, isotopic, and spectroscopic evidence that surface methoxides are the predominant DME-derived intermediates during methylation reactions under their study conditions (similar to ours). With these assumptions, the mechanism-derived rate expression (eq 1) is reduced to

$$\frac{r_{iX}}{[L]} = \frac{k_{iX}K_C K_M K_A \frac{P_{DME}}{P_{MeOH}} P_{Toluene}}{K_M K_A \frac{P_{DME}}{P_{MeOH}} + K_C K_M K_A \frac{P_{DME}}{P_{MeOH}} P_{Toluene}} \quad (2)$$

eq 2 can be recast in terms of only $P_{Toluene}$, k_{iX}, and K_C to obtain a simplified rate equation

$$\frac{r_{iX}}{[L]} = \frac{k_{iX}K_C P_{Toluene}}{1 + K_C P_{Toluene}} \quad (3)$$

$$k_{totalX} = k_{pX} + k_{oX} + k_{mX} \quad (4)$$

which describes the transition in individual xylene formation rates (Figures S14b and S15b, Supporting Information) and total xylene formation rates (Figure 4A) from first- to zero-order in toluene pressure ($P_{Toluene}$) to reflect increasing coverages of toluene coadsorbed on sites covered with DME-derived C_1 species, such as surface methoxy (CH_3–Z). Kinetic fits for three representative samples give similar K_C values (within 1.4×, Figure 4B and Table S4, Supporting Information). In contrast, total xylene formation rate constants (k_{totalX}; eq 4) are 7× smaller on MFI-EDA-1 and MFI-DABCO-1 than on MFI-TPA-C (Figure 4B and Table S4, Supporting Information); specifically, k_{pX} is 2–3× smaller, while k_{mX} and k_{oX} are 20–40× smaller on MFI-EDA-1 and MFI-DABCO-1 than on MFI-TPA-C (Table S4, Supporting Information). Thus, rate constants for forming *m*-X and *o*-X are preferentially lower, by an order-of-magnitude, than those for *p*-X on MFI-EDA-1 and MFI-DABCO-1 relative to MFI-TPA-C, leading to k_{pX}/k_{oX} ratios that are 10–14× larger. The ability of eq 3 to describe experimental rate data and the similar K_C values among the various MFI samples indicate that their kinetic differences reflect different transition state stabilities to form each xylene isomer, as opposed to changes in reaction mechanism or stabilities of reaction intermediates.

2.2. Toluene Methylation Selectivities Are Sensitive to Transition State Environments in MFI. Transition state theory formalisms[47,48] describe the rate constant to form each xylene isomer (k_{iX}) in terms of the Gibbs free energy barrier ($\Delta G_{act,iX}$) to form the transition state from the precursor (i.e., toluene-C_1 coadsorbed species) while accounting for the number of equivalent ring positions ($n_{C-C,i}$) in toluene that can form each isomer (further discussed in Section S5.8, Supporting Information)

$$k_{iX} = n_{C-C,i}\frac{k_B T}{h} e^{-\Delta G_{act,iX}/RT} \quad (5)$$

where *h* and k_B represent Planck's and Boltzmann's constants, respectively. Rate constant ratios (k_{iX}/k_{jX})

$$\frac{k_{iX}}{k_{jX}} = \frac{n_{C-C,i}}{n_{C-C,j}} e^{-\Delta\Delta G_{iX-jX}/RT} \quad (6)$$

reflect Gibbs free energy differences between xylene formation transition states ($\Delta\Delta G_{iX-jX}$) and are independent of the precursor state, which is identical for all three regioisomers regardless of the choice of reaction mechanism (sequential or concerted).[44] The measured $\Delta\Delta G_{pX-oX}$ ($\Delta\Delta G_{pX-oX,exp}$) value is ~1 kJ mol^{-1} on MFI-TPA-C (Table S5, Supporting Information), consistent with a k_{pX}/k_{oX} ratio (0.4) that is nearly 0.5 and with electrophilic aromatic substitution patterns determined by resonance and inductive effects.[28] In contrast, $\Delta\Delta G_{pX-oX,exp}$ is −8 kJ mol^{-1} on MFI-EDA-1 and −7 kJ mol^{-1}

https://doi.org/10.1021/jacs.4c00373
J. Am. Chem. Soc. 2024, 146, 10666–10678

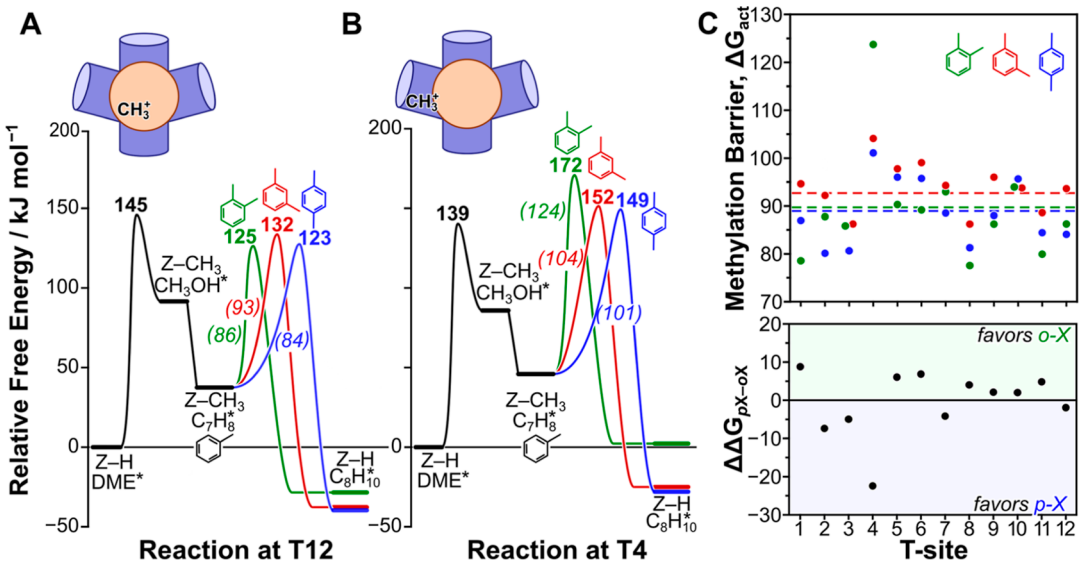

Figure 5. DFT calculated toluene methylation barriers in MFI at distinct T-sites. Reaction coordinate diagram for toluene methylation with DME at (A) T12 and (B) T4 sites of MFI. Effective (bold) and intrinsic (italics) barriers for toluene methylation are shown for *o*-X (green), *m*-X (red), and *p*-X (blue). (C) Intrinsic free energy barriers (ΔG_{act}, kJ mol^{-1}) for toluene methylation to *o*-X, *m*-X, and *p*-X (top) and relative activation barriers ($\Delta\Delta G_{pX\text{-}oX}$, kJ mol^{-1}) between *p*-X and *o*-X (bottom) across all 12 T-sites in MFI zeolites. Dashed lines represent average barriers across the 12 T-sites. Free energies are reported at 403 K, 1 bar.

on MFI-DABCO-1 (Table S5, Supporting Information), leading to higher *p*-X selectivities on those materials.

Toluene methylations to form *o*-X, *m*-X, and *p*-X via DME-derived surface methoxy species (Z−CH_3) were modeled by DFT (described in Section S4, Supporting Information) for the 12 T-sites in MFI zeolites (Figure S48, Supporting Information). All 48 potential T−O site pairs were considered, although three O atoms were excluded because they are inaccessible to toluene. A reaction coordinate diagram for toluene methylation at the T12 of MFI, a stable Al location preferred during synthesis by TPA^+,[12] is shown in Figure 5A. DME binds strongly to H^+ sites ($\Delta G_{ads,DFT}$ = −55 kJ mol^{-1}, Figure S46, Supporting Information) and methylates the surface with a barrier of 145 kJ mol^{-1}. Following methanol desorption and toluene adsorption, toluene methylation occurs with effective barriers (referenced to adsorbed DME*; Figure 5A) of 125, 132, and 123 kJ mol^{-1} for *o*-X, *m*-X, and *p*-X, respectively, suggesting a similar preference for *o*-X and *p*-X formation. These energies reflect the lowest−energy transition states for each reaction with Al at the T12 position out of ∼800 optimized structures generated through extensive sampling of the pore structure around the T12 position (visualized in Figure S49 and the method described in Section S4, Supporting Information). Toluene methylation proceeds via S_N2-like transition states (Figure S61, Supporting Information) containing a planar CH_3^+ carbocation between a ring-C atom of toluene and the O_f, which are located within the MFI intersection in this example.

Effective toluene methylation barriers (referenced to DME*) at T4 (Figure 5B) are much higher than those at T12 and were 172, 152, and 149 kJ mol^{-1} for *o*-X, *m*-X, and *p*-X, respectively, suggesting a strong preference for *p*-X over *o*-X. Transition states at T4 are geometrically similar to those at T12 (Figure S53, Supporting Information), suggesting that barrier differences arise from confinement effects, as acid strengths are similar among different T-sites in MFI.[49] Like at T12, these transition states reflect the most stable among many optimized structures (∼1200 for T4) generated through extensive sampling of the nearby pore network (Figure S49, Supporting Information). Acid sites at T4, unlike most T-sites in the MFI, cannot readily access channel intersections. Therefore, transition states at T4 are confined well within the 10-MR borders of the sinusoidal channel (4.8−6.0 Å from the center of intersection), in contrast to T12, whose transition states are confined within the intersection (1.9−2.6 Å from the center). These effective barriers suggest high *p*-X selectivity relative to *o*-X at T4 and low *p*-X selectivity at T12. Furthermore, effective barriers at T12 are 123−132 kJ mol^{-1} for the three isomers, while those at T4 are 149−172 kJ mol^{-1}, suggesting that rates at T4 would be lower than those at T12. This decrease in the rate with increases in *p*-X selectivity is consistent with the kinetic behavior, as discussed above.

T4, as stated earlier, is unique in its inability to host a proton that resides in the MFI channel intersection; indeed, its predicted selectivity patterns are unique among all 12 T-sites in MFI. Figure 5C shows that intrinsic xylene formation barriers can vary up to 30 kJ mol^{-1} across the 12 T-sites in MFI. Overall, average barriers across the 12 T-sites are, respectively, 89, 94, and 88 kJ mol^{-1} for *o*-X, *m*-X, and *p*-X, with the nearly identical barriers for *o*-X and *p*-X consistent with a 2:1 product ratio due to symmetry differences in toluene. Despite variations in individual barriers, differences in DFT-calculated barriers between *p*-X and *o*-X are small ($|\Delta\Delta G_{pX-oX,DFT}| \leq 5$ kJ mol^{-1}) for 8 of the 12 T-sites in MFI, with T4 being the most notable outlier. Like for T4 and T12, data at all T-sites reflect the lowest-energy transition states isolated through extensive sampling of the pore network, resulting in ∼19,000 converged transition state structures. These data suggest that the environment surrounding the location of the reactive intermediate (e.g., surface methoxy) that methylates toluene is crucial in determining the relative barriers to the formation of xylene isomers.

$\Delta\Delta G_{pX-oX,DFT}$ values across the 45 accessible T−O site-pairs indicate that surface methoxy species located on O atoms

https://doi.org/10.1021/jacs.4c00373
J. Am. Chem. Soc. 2024, 146, 10666−10678

within sinusoidal or straight channels strongly favor *p*-X formation over *o*-X, while methoxy species within channel intersections show a weak preference for *o*-X (Figure 6A).

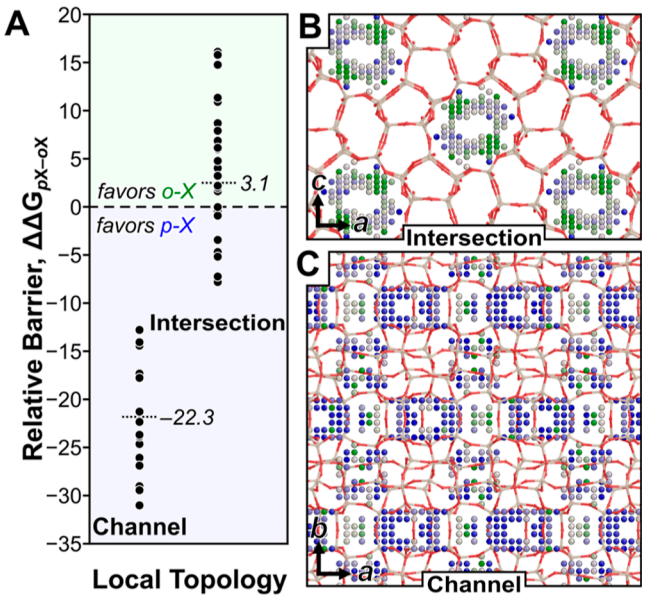

Figure 6. (A) DFT-calculated $\Delta\Delta G_{pX-oX}$ values for toluene methylation at 48 T−O site-pairs (surface methyl locations) organized by whether the O atoms are accessible to the intersection or only accessible to either the straight or sinusoidal channel. Free energies are reported at 403 K, 1 bar. Locations of CH_3^+ species for transition states at (B) intersections (shown for a−c plane) and (C) channels (shown for a,b plane) within MFI with the color representing the local $\Delta\Delta G_{pX-oX}$ value (blue: ≤−20 kJ mol^{-1}, white: = 0 kJ mol^{-1}, and green: ≥20 kJ mol^{-1}, with gradients between those values).

Barriers to form *p*-X in channels are 13−31 kJ mol^{-1} lower than those to form *o*-X (average of −22 kJ mol^{-1}, strongly favoring *p*-X), while barriers range from 8 kJ mol^{-1} lower to 16 kJ mol^{-1} greater for *p*-X relative to *o*-X in intersections (average of 3 kJ mol^{-1}, slightly favoring *o*-X). Transition states with CH_3^+ species in MFI intersections (Figure 6B) show mostly unselective behavior, while those inside MFI channels (Figure 6C) predominantly favor *p*-X formation (as indicated by mostly blue dots). Effective barriers are higher in channels than in intersections for all three xylene isomers (Figures S62, Supporting Information), but *o*-X formation is disproportionately disfavored over *p*-X formation in channels, leading to increased p-X selectivity. Furthermore, these shifts in free energy (Figures 5, 6 and Figure S62, Supporting Information) are consistent with those in enthalpy (Figure S47, Supporting Information), indicating that these trends are driven by enthalpic rather than entropic effects associated with confinement. These theoretical data showing higher *p*-X selectivities and lower rates for reactions within channels rather than in intersection environments in MFI suggest that those behaviors observed in MFI synthesized with nonconventional SDAs can be caused by changes in Al site distributions that shift toluene methylation to occur within channels.

2.3. Organic SDAs Bias Al Distribution within MFI. Previous theoretical and NMR studies[12−16,50] have revealed that OSDAs, typically quaternary alkylammonium or non-quaternary alkylamine molecules, interact with Al atoms in aluminosilicate frameworks via electrostatic interactions. These Coulombic interactions influence Al siting at lattice positions close to the charged nitrogen (N^+) centers of the occluded OSDA. Our recent DFT studies[12] reveal that occluded TPA^+ positions its N^+ at MFI intersections, which energetically prefers Al siting at T-site bordering channel intersections (Figure 1D). In contrast to TPA^+, EDA and DABCO contain N atoms at their periphery (Figure 1E) and are flexible to orient their N atoms toward T-sites within channels, which we hypothesized may bias Al distributions. With the exception of MFI-TPA-3 containing relatively high Na^+ content (2.4 Na^+ per unit cell), all as-synthesized MFI samples contained low (or no) Na^+ content (0.0−1.1 Na^+ per unit cell; Table S9, Supporting Information), indicating that the majority (>50%) of framework Al centers (1.6−2.2 Al per unit cell; Table 1) are charge compensated by organic SDAs (≥4 molecules per unit cell; Table S9, Supporting Information) in these samples; excess cationic charges are expected to balance ≡SiO^- defects to maintain overall framework charge neutrality. Solid-state ^{27}Al NMR was used to probe the distributions of tetrahedrally coordinated Al in the frameworks of MFI synthesized with TPA^+ and nonconventional OSDAs. ^{27}Al MAS NMR spectra showed qualitative differences in spectral features that support the presence of different framework Al distributions among these samples (additional details in Section S5.12, Supporting Information); however, given the well-documented challenges in resolving Al T-site assignments in the low-symmetry MFI framework using NMR,[50−54] we turned to DFT to assess plausible locations of occluded SDAs and their influence on the energetics of siting Al among different T-sites in MFI.

Our prior DFT work assessing TPA^+ as the SDA[12] revealed that the preference of siting Al among the 12 T-sites in MFI depends on the relative intrinsic stabilities of Al substitution at each of those positions and the Coulombic interaction between the cationic SDA and the anionic $[AlO_{4/2}]^-$ centers governed by N−Al distances. T12 has the lowest intrinsic (SDA-free) stability for Al substitution and is relatively close (5.1 Å) to the cationic N^+ center in occluded TPA^+. Thus, both factors contribute to a strong thermodynamic preference for Al siting at T12 in the presence of TPA^+, with Al siting energies that are 12−34 kJ mol^{-1} higher at the other 11 T-sites (Figure 7C). Although our DFT analysis focuses on thermodynamic factors, which neglect potential kinetic impacts on Al siting and omit key details of the hydrothermal synthesis conditions (e.g., solvent effects), this analysis is among the current state-of-the-art approaches for investigating SDA-framework Al interactions. Here, we examine how protonated DABCO complexes provide intermolecular interactions in addition to Coulombic interactions to influence Al siting.

The crystallization of MFI-DABCO is performed with a 1:1 ratio of DABCO/MA in water. DABCO, unlike TPA^+, is neutral, and upon protonation, it can form strong H-bonds to either MA or H_2O, depending on the intrapore MA/H_2O ratio. Thus, we computed the energy to substitute Al at all framework positions around protonated complexes between DABCO and MA (DABCO−H−MA^+) or H_2O (DABCO−H−H_2O^+), with three neutral DABCO−MA(H_2O) complexes in the other intersections (details in Sections S4 and S5.21, Supporting Information). While TPA^+ is constrained by the MFI topology such that its N^+ center resides near the center of the intersection, a protonated DABCO complex can rotate within the intersection such that its charged center can be oriented close to adjacent channels (Figure 7A,B and Figures S77−S80, Supporting Information). This flexibility permits the

https://doi.org/10.1021/jacs.4c00373
J. Am. Chem. Soc. 2024, 146, 10666−10678

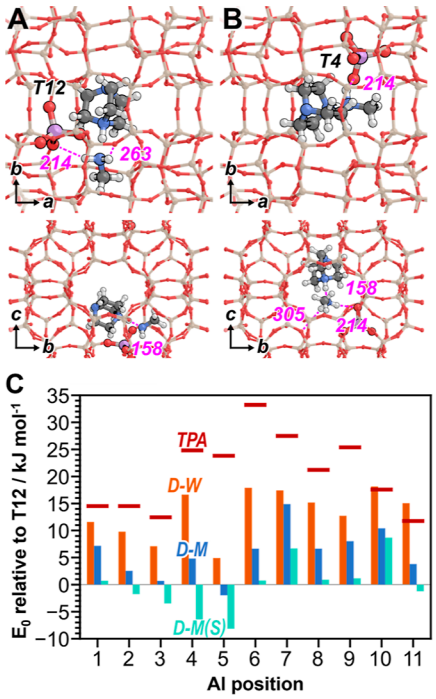

Figure 7. OSDA−Al interactions in the MFI lattice. Protonated DABCO−MA complex interacting with Al at (A) T12 and (B) T4. H-bonds are shown in dashed lines, with distances shown in pm. (C) Energies (E_0) of Al in positions T1−T11 (relative to T12) with varying SDA complexes: TPA (1 TPA^+; horizontal red dashes; adapted from Nimlos et al.[12]), DABCO−water complex (D-W, 4 DABCO, 4 H_2O, one DABCO−H_2O complex is protonated; orange bars), DABCO−MA (D-M, 4 DABCO, 4 MA, one DABCO−MA complex protonated; blue bars), and DABCO−MA with VASPsol (D-M(S); teal bars).

formation of H-bonds, facilitated by MA or H_2O, to the O atoms at T-sites more distant than those located at the intersection border. This H-bonding chain connects the tertiary amine in DABCO directly to the Al site; this interaction is present for all 12 T-sites, even T4, which is farthest from the intersection center (7.8 Å; Figure 7B).

The ability of DABCO to reorient within intersections and engage in H-bonding interactions with distant O_f atoms render this SDA more flexible than TPA^+. These abilities allow DABCO to stabilize a broader range of Al locations than TPA^+, as shown by Al siting energies (reflecting the most-stable framework position for each T-site out of the 96 considered) for DABCO−H−H_2O^+ at T1−T11 that are only 4−22 kJ mol^{-1} less stable than T12 (Figure 7C and Figures S79 and S80, Supporting Information); for TPA^+, this range was 12−34 kJ mol^{-1} less stable than T12. For DABCO−H−MA^+ complexes, the effect is even stronger because MA is a stronger base than H_2O and facilitates the H^+ shifting to MA, serving to extend the cationic center of the complex closer to O_f atoms located further from the intersection. Thus, when DABCO−H−MA^+ is the SDA, energies for Al siting range from 2 kJ mol^{-1} more stable (T5) to 15 kJ mol^{-1} less stable (T7) than for T12, predicting more evenly distributed Al atoms among available T-sites. Our prior work[12] showed that including an implicit solvation model decreased the impact of charge separation and resulted in a slight decrease in the preference for TPA^+ to site Al at T12 (energies 10−28 kJ mol^{-1} less stable than T12 with solvation and 12−34 kJ mol^{-1} without solvation). With DABCO−H−MA^+, the same implicit solvation method strongly favors Al siting at T4 and T5 (6 and 8 kJ mol^{-1} more stable than T12) (Figure 7C and Figures S77 and S78, Supporting Information).

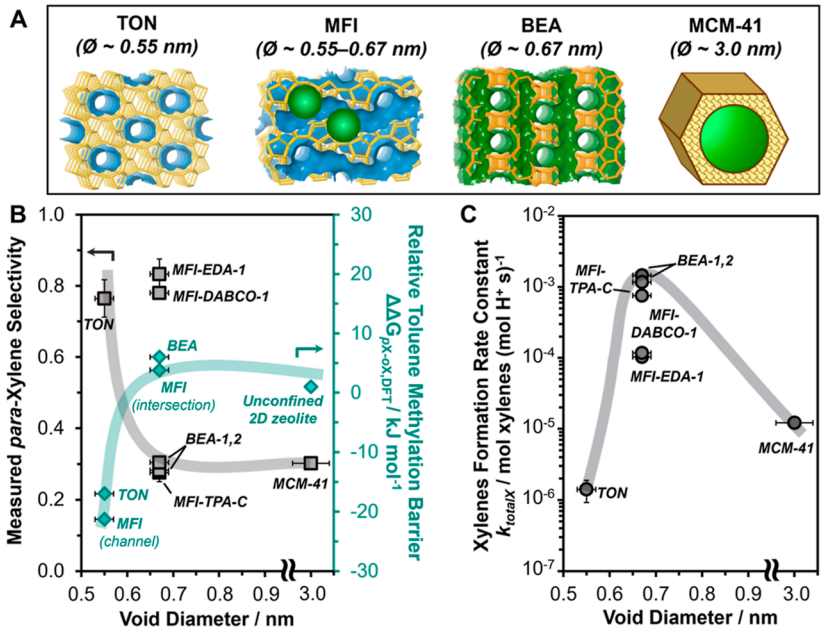

Figure 8. Toluene methylation across aluminosilicates with varying void sizes. (A) Framework topology of TON, MFI, BEA,[5] and MCM-41. (B) Average measured *p*-X selectivity (squares; 403 K, 0.2−8.8 kPa toluene, 66 kPa DME) and average DFT-calculated toluene methylation activation barriers for *p*-X relative to *o*-X ($\Delta\Delta G_{pX\text{-}oX,DFT}$; diamonds; 403 K, 1 bar; details in Section S5.20, Supporting Information) as a function of largest cavity void diameter in the aluminosilicate; uncertainties in *p*-X selectivity represent one standard deviation of average measured *p*-X selectivity across the range of toluene pressures. (C) Total xylene formation rate constant (k_{totalX}; 403 K) as a function of void diameter; error bars in the total xylene formation rate constant represent the 95% confidence interval. Uncertainties in the void sizes are ±0.02 nm. Lines serve to guide the eye.

https://doi.org/10.1021/jacs.4c00373
J. Am. Chem. Soc. 2024, 146, 10666−10678

As described earlier, T4 is the most selective T-site for *p*-X formation, and Al exchange at this position goes from being 25 kJ mol^{-1} less stable than T12 using TPA^+ to 5 kJ mol^{-1} less stable (without solvation) or 6 kJ mol^{-1} more stable (with solvation) using DABCO−H−MA^+ (Figure 7C). This shift is among the largest observed across the 12 T-sites in MFI, indicating that the flexibility of DABCO SDAs most benefits the hardest-to-reach environment within MFI (T4). These findings are consistent with prior reports on FER zeolites, where quaternary ammonium OSDAs and nonquaternary amine OSDA-bearing protons on their periphery that are flexible and able to form strong H-bonds with O_f atoms show different biases in Al distributions[13,55] and concomitant changes in DME carbonylation rates.[56] Our observations are also consistent with a recent computational study (DFT and *ab initio* molecular dynamics) on MFI zeolites, where OSDAs with different charge distributions and mobility within voids can bias the Al siting toward T-sites away from MFI intersections.[57] Although we did not examine the role of EDA in Al siting during our "mixed-template" synthesis of MFI, earlier reports[58,59] suggest that protonated EDA molecules are stabilized by favorable van der Waals interactions within the smaller sinusoidal and straight channels of MFI (compared to larger intersection voids), consistent with a shift in Al distribution toward channel environments. Our analysis of OSDA-framework Al interactions, when combined with experimental and DFT data on how rate and selectivity depend on reaction environment in MFI, further corroborates the hypothesis that MFI synthesized by nonconventional OSDAs yield materials with larger fractions of H^+ sites in channel environments.

2.4. Void Sizes within Brønsted Acid Aluminosilicates Dictate Rate and Isomer Selectivity. Both experiment and theory indicate that more tightly confined locations in MFI channels preferentially form *p*-X over *o*-X and *m*-X, compared to the more spacious intersections, which show little preference for stabilizing transition states that form *o*-X or *p*-X. Given the well-known challenges to precisely quantify H^+ sites located in intersections or channels of MFI,[8,51,52] we further tested our hypotheses related to confinement-induced transition state selectivity by examining other microporous aluminosilicates containing void environments of more uniform sizes and similar to those found in MFI zeolites (Figure 8A). TON is a one-dimensional zeolite with a micropore diameter (∼0.55 nm) similar to that of MFI channels (∼0.55 nm), while BEA is a three-dimensional zeolite with a micropore diameter (∼0.67 nm) similar to that of MFI intersections (∼0.67 nm).[5,60] MCM-41 is a mesoporous aluminosilicate with cylindrical channels that are ∼3.0 nm in diameter, without smaller micropores, and is representative of acid sites in unconfined locations. Prior work[49,61] has reported that Brønsted acid strength (i.e., deprotonation energy) does not vary among zeolites and mesoporous aluminosilicates. All samples showed similar kinetic and mechanistic behavior with reactant pressures (Section S5.6 and Figures S14−S19, Supporting Information); thus, any differences in reactivity and selectivity among these materials should reflect the pore-confinement effects on the kinetically relevant transition states to form xylenes.

The selectivity to *p*-X decreases with increasing void diameter (Figure 8B) from ∼80% (∼0.55 nm; TON) to 30% (∼0.67 nm; BEA) and is invariant with further increases in void size (∼3.0 nm; MCM-41). MFI-TPA-C shows *p*-X selectivity similar to that of BEA, while MFI-EDA-1 and MFI-DABCO-1 show *p*-X selectivity (∼80%) similar to that of TON (∼0.55 nm). Experimentally measured selectivities (Figure 8B and Figures S14−S19) and $\Delta\Delta G_{pX-oX,exp}$ values (Table S5) are supported by $\Delta\Delta G_{pX-oX,DFT}$ values for TON and BEA, and on a "surface-like" (2D) zeolite model used to represent an unconfined Brønsted acid site in MCM-41 (Figure 8B, Section S5.20, and Figures S63−S76, Supporting Information). TON has four T-sites, three of which are accessible to toluene methylation transition states; barriers are lower to form *p*-X than *o*-X at all three T-sites (avg. $\Delta\Delta G_{pX-oX,DFT}$ = −17 kJ mol^{-1}), in qualitative agreement with the −24 kJ mol^{-1} lower value for T4 in MFI and consistent with the higher *p*-X selectivity and $\Delta\Delta G_{pX-oX,exp}$ (−6 kJ mol^{-1}) observed for TON (Figure 8B). BEA has 9 T-sites, and $\Delta\Delta G_{pX-oX,DFT}$ across those sites range from −2 to +8 kJ mol^{-1}, with an average of +4 kJ mol^{-1}, while the unconfined 2D model has a $\Delta\Delta G_{pX-oX,DFT}$ of +1 kJ mol^{-1}, consistent with the lower *p*-X selectivity and $\Delta\Delta G_{pX-oX,exp}$ (∼0 kJ mol^{-1}) for both BEA and MCM-41 (Figure 8B).

Furthermore, values of k_{totalX} among aluminosilicates show a nonmonotonic dependence on their largest cavity diameter (Figure 8C and Table S4, Supporting Information), with values on TON and MCM-41 that were, respectively, ∼500× and ∼60× lower than on MFI-TPA-C (Figure 8C); such dependencies on aluminosilicate void size have been previously reported for various acid-catalyzed reactions,[62−66] reflecting more effective transition state stabilization as the pore size decreases to approach that of the transition state, but more severe destabilization of the transition state with further decreases in pore size. Values of k_{totalX} on MFI-TPA-C were similar to those on BEA (within 1.8×, Figure 8C); yet, values of k_{totalX} on MFI-EDA-1 and MFI-DABCO-1 were 12−13× smaller (Figure 8C) than those on BEA. Taken together, the rate and selectivity trends across aluminosilicates with varying void sizes are consistent with MFI zeolites synthesized using TPA^+, containing H^+ sites predominantly located within channel intersections, while MFI zeolites synthesized using EDA or DABCO contain a larger fraction of H^+ sites located within more constrained channel environments.

3. CONCLUSIONS

We conclude from the combined experimental and theoretical data that MFI zeolites synthesized using nonconventional organic SDAs (DABCO, MA, and EDA) contain significant fractions of framework Al (and associated H^+) sites located within more confined channels. Such voids destabilize toluene methylation transition states that form all xylene isomers but less so for the smaller (desired) isomer, thus leading to lower overall xylene formation rates and higher intrinsic *p*-X selectivities.

These findings demonstrate how synthetic strategies that harness different intermolecular interactions (e.g., electrostatics and H-bonding) between N^+ centers in OSDAs and $AlO_{4/2}^-$ in lattices enable tuning of active site distributions during zeolite crystallization for an industrially relevant material (MFI), with direct consequences for regioisomer product selectivity in an industrially relevant catalytic reaction (*p*-X formation). This approach opens new and orthogonal design strategies to broaden catalytic diversity in zeolitic materials different from those derived using conventional wisdom[26,29−31] that otherwise optimize coupled reaction-transport phenomena to increase regioisomer selectivity.

https://doi.org/10.1021/jacs.4c00373
J. Am. Chem. Soc. 2024, 146, 10666−10678

Furthermore, the synthetic placement of active sites within desired pore environments of a given zeolite is complementary to postsynthetic approaches that selectively eliminate active sites in undesired pore environments through *ex situ* poisoning before catalysis or *in situ* deactivation during catalysis,[33,67,68] and approaches that selectively replace heteroatoms of lower reactivity (e.g., B) with those of higher reactivity (e.g., Al) within specific pore environments.[69] The resulting insights from our study have broader implications in catalyst design for a wide range of reactions, including the selective upgrading of traditional fossil feedstocks (crude oil and shale gas) and emerging feedstocks (biomass and waste plastics).

■ ASSOCIATED CONTENT

Supporting Information

The Supporting Information is available free of charge at https://pubs.acs.org/doi/10.1021/jacs.4c00373.

Materials and methods and synthesis and characterization of MFI zeolites, toluene methylation kinetic studies, and DFT studies (PDF)

■ AUTHOR INFORMATION

Corresponding Authors

David Hibbitts − *Department of Chemical Engineering, University of Florida, Gainesville, Florida 32608, United States;* orcid.org/0000-0001-8606-7000; Email: rgounder@purdue.edu

Rajamani Gounder − *Davidson School of Chemical Engineering, Purdue University, West Lafayette, Indiana 47907, United States;* orcid.org/0000-0003-1347-534X; Email: hibbitts@ufl.edu

Authors

Sopuruchukwu Ezenwa − *Davidson School of Chemical Engineering, Purdue University, West Lafayette, Indiana 47907, United States*

Hansel Montalvo-Castro − *Department of Chemical Engineering, University of Florida, Gainesville, Florida 32608, United States;* orcid.org/0000-0001-8833-7668

Alexander J. Hoffman − *Department of Chemical Engineering, University of Florida, Gainesville, Florida 32608, United States;* orcid.org/0000-0002-1337-9297

Huston Locht − *Department of Chemical Engineering, University of Florida, Gainesville, Florida 32608, United States*

Jordan Attebery − *Department of Chemical Engineering, University of Florida, Gainesville, Florida 32608, United States*

Deng-Yang Jan − *Honeywell UOP, Des Plaines, Illinois 60017, United States*

Michael Schmithorst − *Department of Chemical Engineering, University of California, Santa Barbara, Santa Barbara, California 93106, United States;* orcid.org/0000-0002-8795-5082

Bradley Chmelka − *Department of Chemical Engineering, University of California, Santa Barbara, Santa Barbara, California 93106, United States*

Complete contact information is available at: https://pubs.acs.org/10.1021/jacs.4c00373

Funding

Financial support was provided in part by Honeywell UOP (R.G. and S.E.) and in part by the U.S. National Science Foundation (NSF) under Cooperative Agreement no. EEC-1647722, which is an Engineering Research Center for the Innovative and Strategic Transformation of Alkane Resources (R.G. and S.E.). Financial support was provided by the NSF CAREER program under award 1942684-CBET (D.H., A.J.H., H.M., H.L., and J.A.). This work was supported by computational resources from both the Extreme Science and Engineering Discovery Environment (XSEDE), which is supported by the NSF grant no. ACI-1548562 through allocation CTS160041, and the University of Florida Research Computing (D.H., A.J.H., H.M., H.L., and J.A.). NMR measurements were conducted with financial support from BASF using the shared facilities of the Materials Research Science and Engineering Center (MRSEC) at UC Santa Barbara, which are supported by the NSF under Award no. DMR 2308708; the UC Santa Barbara MRSEC is a member of the NSF-funded Materials Research Facilities Network (http://www.mrfn.org) (B.C. and M.S.).

Notes

The authors declare the following competing financial interest(s): A US patent application 18/176,465 titled MFI Zeolite of Highly Dispersed Framework Aluminum and its Uses for Selective Aromatics Methylation to para-Xylene (inventors: D.-Y.J, R.G., S.E., J.G.M. (Jamie G. Moscoso), G.Z. (Gregory Kuzmanich); applicant: UOP LLC) was filed on Feb 28, 2023, and claims priority over our earlier US provisional application 63/315,429 filed on March 1, 2022.

■ ACKNOWLEDGMENTS

The authors acknowledge Y. G. Hur, B. J. Lee, P. Kester, C. Nimlos, and S. Lee for synthesizing some of the MFI samples used in this study. The authors also acknowledge S. Lee and M. DeLuca for helpful technical discussions.

■ REFERENCES

(1) Martínez, C.; Corma, A. Inorganic Molecular Sieves: Preparation, Modification and Industrial Application in Catalytic Processes. *Coord. Chem. Rev.* **2011**, *255* (13−14), 1558−1580.

(2) Venuto, P. B. Organic Catalysis over Zeolites: A Perspective on Reaction Paths within Micropores. *Microporous Mesoporous Mater.* **1994**, *2* (5), 297−411.

(3) Pérez-Botella, E.; Valencia, S.; Rey, F. Zeolites in Adsorption Processes: State of the Art and Future Prospects. *Chem. Rev.* **2022**, *122* (24), 17647−17695.

(4) Degnan, T. F. The Implications of the Fundamentals of Shape Selectivity for the Development of Catalysts for the Petroleum and Petrochemical Industries. *J. Catal.* **2003**, *216* (1−2), 32−46.

(5) Baerlocher, C.; McCusker, L. B. Database of Zeolite Structures. http://www.iza-structure.org/databases/ (accessed Nov 11, 2019).

(6) Pophale, R.; Cheeseman, P. A.; Deem, M. W. A Database of New Zeolite-like Materials. *Phys. Chem. Chem. Phys.* **2011**, *13* (27), 12407−12412.

(7) Zones, S. I. Translating New Materials Discoveries in Zeolite Research to Commercial Manufacture. *Microporous Mesoporous Mater.* **2011**, *144* (1−3), 1−8.

(8) Knott, B. C.; Nimlos, C. T.; Robichaud, D. J.; Nimlos, M. R.; Kim, S.; Gounder, R. Consideration of the Aluminum Distribution in Zeolites in Theoretical and Experimental Catalysis Research. *ACS Catal.* **2018**, *8* (2), 770−784.

(9) Dědeček, J.; Tabor, E.; Sklenak, S. Tuning the Aluminum Distribution in Zeolites to Increase Their Performance in Acid-Catalyzed Reactions. *ChemSusChem* **2019**, *12* (3), 556−576.

(10) Gounder, R.; Iglesia, E. The Catalytic Diversity of Zeolites: Confinement and Solvation Effects within Voids of Molecular Dimensions. *Chem. Commun.* **2013**, *49* (34), 3491−3509.
(11) Hoffman, A. J.; Bates, J. S.; Di Iorio, J. R.; Nystrom, S. V.; Nimlos, C. T.; Gounder, R.; Hibbitts, D. Rigid Arrangements of Ionic Charge in Zeolite Frameworks Conferred by Specific Aluminum Distributions Preferentially Stabilize Alkanol Dehydration Transition States. *Angew. Chem., Int. Ed.* **2020**, *59* (42), 18686−18694.
(12) Nimlos, C. T.; Hoffman, A. J.; Hur, Y. G.; Lee, B. J.; Di Iorio, J. R.; Hibbitts, D. D.; Gounder, R. Experimental and Theoretical Assessments of Aluminum Proximity in MFI Zeolites and Its Alteration by Organic and Inorganic Structure-Directing Agents. *Chem. Mater.* **2020**, *32* (21), 9277−9298.
(13) Pinar, A. B.; Gómez-Hortigüela, L.; McCusker, L. B.; Pérez-Pariente, J. Controlling the Aluminum Distribution in the Zeolite Ferrierite via the Organic Structure Directing Agent. *Chem. Mater.* **2013**, *25* (18), 3654−3661.
(14) Muraoka, K.; Chaikittisilp, W.; Yanaba, Y.; Yoshikawa, T.; Okubo, T. Directing Aluminum Atoms into Energetically Favorable Tetrahedral Sites in a Zeolite Framework by Using Organic Structure-Directing Agents. *Angew. Chem., Int. Ed.* **2018**, *57* (14), 3742−3746.
(15) Wang, Z.; Chu, W.; Zhao, Z.; Liu, Z.; Chen, H.; Xiao, D.; Gong, K.; Li, F.; Li, X.; Hou, G. The Role of Organic and Inorganic Structure-Directing Agents in Selective Al Substitution of Zeolite. *J. Phys. Chem. Lett.* **2021**, *12* (38), 9398−9406.
(16) Shantz, D. F.; Lobo, R. F.; Fild, C.; Koller, H. Controlling the Distribution of Framework Aluminum in High-Silica Zeolites. In *Studies in Surface Science and Catalysis*; Corma, A., Melo, F. V., Mendioroz, S., Fierro, J. L. G., Eds.; 12th International Congress on Catalysis; Elsevier, 2000; Vol. *130*, pp 845−850.
(17) Yokoi, T.; Mochizuki, H.; Namba, S.; Kondo, J. N.; Tatsumi, T. Control of the Al Distribution in the Framework of ZSM-5 Zeolite and Its Evaluation by Solid-State NMR Technique and Catalytic Properties. *J. Phys. Chem. C* **2015**, *119* (27), 15303−15315.
(18) Biligetu, T.; Wang, Y.; Nishitoba, T.; Otomo, R.; Park, S.; Mochizuki, H.; Kondo, J. N.; Tatsumi, T.; Yokoi, T. Al Distribution and Catalytic Performance of ZSM-5 Zeolites Synthesized with Various Alcohols. *J. Catal.* **2017**, *353*, 1−10.
(19) Liu, H.; Wang, H.; Xing, A.-H.; Cheng, J.-H. Effect of Al Distribution in MFI Framework Channels on the Catalytic Performance of Ethane and Ethylene Aromatization. *J. Phys. Chem. C* **2019**, *123* (25), 15637−15647.
(20) Ma, J.; Hidaka, K.; Ogura, M.; Moteki, T. Experimental Evidence for the Relationship between Al Site Distribution and Catalytic Performance in Methanol-to-Olefins Reaction over ZSM-5 Zeolite. *Cryst. Growth Des.* **2023**, *23* (12), 8499−8508.
(21) Gallego, E. M.; Portilla, M. T.; Paris, C.; León-Escamilla, A.; Boronat, M.; Moliner, M.; Corma, A. Ab Initio" Synthesis of Zeolites for Preestablished Catalytic Reactions. *Science* **2017**, *355* (6329), 1051−1054.
(22) Li, C.; Paris, C.; Martínez-Triguero, J.; Boronat, M.; Moliner, M.; Corma, A. Synthesis of Reaction-adapted Zeolites as Methanol-to-Olefins Catalysts with Mimics of Reaction Intermediates as Organic Structure-directing Agents. *Nat. Catal.* **2018**, *1* (7), 547−554.
(23) Schwalbe-Koda, D.; Kwon, S.; Paris, C.; Bello-Jurado, E.; Jensen, Z.; Olivetti, E.; Willhammar, T.; Corma, A.; Román-Leshkov, Y.; Moliner, M.; Gómez-Bombarelli, R. A Priori Control of Zeolite Phase Competition and Intergrowth with High-Throughput Simulations. *Science* **2021**, *374* (6565), 308−315.
(24) Li, C.; Ferri, P.; Paris, C.; Moliner, M.; Boronat, M.; Corma, A. Design and Synthesis of the Active Site Environment in Zeolite Catalysts for Selectively Manipulating Mechanistic Pathways. *J. Am. Chem. Soc.* **2021**, *143* (28), 10718−10726.
(25) Ferri, P.; Li, C.; Schwalbe-Koda, D.; Xie, M.; Moliner, M.; Gómez-Bombarelli, R.; Boronat, M.; Corma, A. Approaching Enzymatic Catalysis with Zeolites or How to Select One Reaction Mechanism Competing with Others. *Nat. Commun.* **2023**, *14* (1), 2878.
(26) Chakinala, N.; Chakinala, A. G. Process Design Strategies To Produce P-Xylene via Toluene Methylation: A Review. *Ind. Eng. Chem. Res.* **2021**, *60* (15), 5331−5351.
(27) Chirico, R. D.; Steele, W. V. Thermodynamic Equilibria in Xylene Isomerization. 5. Xylene Isomerization Equilibria from Thermodynamic Studies and Reconciliation of Calculated and Experimental Product Distributions. *J. Chem. Eng. Data* **1997**, *42* (4), 784−790.
(28) Solomons, T. W. G.; Fryhle, C. B.; Snyder, S. A. *Organic Chemistry*, 12th ed.; Wiley Global Education, 2016.
(29) Young, L. B.; Butter, S. A.; Kaeding, W. W. Shape Selective Reactions with Zeolite Catalysts: III. Selectivity in Xylene Isomerization, Toluene-Methanol Alkylation, and Toluene Disproportionation over ZSM-5 Zeolite Catalysts. *J. Catal.* **1982**, *76* (2), 418−432.
(30) Wei, J. A Mathematical Theory of Enhanced Para-Xylene Selectivity in Molecular Sieve Catalysts. *J. Catal.* **1982**, *76* (2), 433−439.
(31) Ahn, J. H.; Kolvenbach, R.; Gutiérrez, O. Y.; Al-Khattaf, S. S.; Jentys, A.; Lercher, J. A. Tailoring P-Xylene Selectivity in Toluene Methylation on Medium Pore-Size Zeolites. *Microporous Mesoporous Mater.* **2015**, *210*, 52−59.
(32) Fraenkel, D. Role of External Surface Sites in Shape-Selective Catalysis over Zeolites. *Ind. Eng. Chem. Res.* **1990**, *29* (9), 1814−1821.
(33) Parmar, D.; Cha, S. H.; Salavati-fard, T.; Agarwal, A.; Chiang, H.; Washburn, S. M.; Palmer, J. C.; Grabow, L. C.; Rimer, J. D. Spatiotemporal Coke Coupling Enhances Para-Xylene Selectivity in Highly Stable MCM-22 Catalysts. *J. Am. Chem. Soc.* **2022**, *144* (17), 7861−7870.
(34) Mirth, G.; Lercher, J. A. On the Role of Product Isomerization for Shape Selective Toluene Methylation over HZSM5. *J. Catal.* **1994**, *147* (1), 199−206.
(35) Bhan, A.; Iglesia, E. A Link between Reactivity and Local Structure in Acid Catalysis on Zeolites. *Acc. Chem. Res.* **2008**, *41* (4), 559−567.
(36) Mirth, G.; Cejka, J.; Lercher, J. A. Transport and Isomerization of Xylenes over HZSM-5 Zeolites. *J. Catal.* **1993**, *139* (1), 24−33.
(37) Hill, I.; Malek, A.; Bhan, A. Kinetics and Mechanism of Benzene, Toluene, and Xylene Methylation over H-MFI. *ACS Catal.* **2013**, *3* (9), 1992−2001.
(38) Allen, R. H.; Yats, L. D. Kinetics of Three-Compound Equilibrations. V. Concurrent Alkylation and Isomerization. *J. Am. Chem. Soc.* **1961**, *83* (13), 2799−2805.
(39) Brown, H. C.; Jungk, H. The Reaction of Benzene and Toluene with Methyl Bromide and Iodide in the Presence of Aluminum Bromide; Evidence for a Displacement Mechanism in the Methylation of Aromatic Compounds. *J. Am. Chem. Soc.* **1955**, *77* (21), 5584−5589.
(40) Yashima, T.; Ahmad, H.; Yamazaki, K.; Katsuta, M.; Hara, N. Alkylation on Synthetic Zeolites: I. Alkylation of Toluene with Methanol. *J. Catal.* **1970**, *16* (3), 273−280.
(41) Wang, C.; Zhang, L.; Huang, X.; Zhu, Y.; Li, G.; Gu, Q.; Chen, J.; Ma, L.; Li, X.; He, Q.; Xu, J.; Sun, Q.; Song, C.; Peng, M.; Sun, J.; Ma, D. Maximizing Sinusoidal Channels of HZSM-5 for High Shape-Selectivity to p-Xylene. *Nat. Commun.* **2019**, *10* (1), 4348.
(42) Karwacki, L.; Kox, M. H. F.; Matthijs de Winter, D. A.; Drury, M. R.; Meeldijk, J. D.; Stavitski, E.; Schmidt, W.; Mertens, M.; Cubillas, P.; John, N.; Chan, A.; Kahn, N.; Bare, S. R.; Anderson, M.; Kornatowski, J.; Weckhuysen, B. M. Morphology-Dependent Zeolite Intergrowth Structures Leading to Distinct Internal and Outer-Surface Molecular Diffusion Barriers. *Nat. Mater.* **2009**, *8* (12), 959−965.
(43) Medeiros-Costa, I. C.; Dib, E.; Nesterenko, N.; Dath, J.-P.; Gilson, J.-P.; Mintova, S. Silanol Defect Engineering and Healing in Zeolites: Opportunities to Fine-Tune Their Properties and Performances. *Chem. Soc. Rev.* **2021**, *50* (19), 11156−11179.
(44) DeLuca, M.; Kravchenko, P.; Hoffman, A.; Hibbitts, D. Mechanism and Kinetics of Methylating C6-C12 Methylbenzenes with Methanol and Dimethyl Ether in H-MFI Zeolites. *ACS Catal.* **2019**, *9* (7), 6444−6460.

https://doi.org/10.1021/jacs.4c00373
J. Am. Chem. Soc. 2024, 146, 10666−10678

(45) Cheung, P.; Bhan, A.; Sunley, G. J.; Law, D. J.; Iglesia, E. Site Requirements and Elementary Steps in Dimethyl Ether Carbonylation Catalyzed by Acidic Zeolites. *J. Catal.* **2007**, *245* (1), 110−123.
(46) Cheung, P.; Bhan, A.; Sunley, G. J.; Iglesia, E. Selective Carbonylation of Dimethyl Ether to Methyl Acetate Catalyzed by Acidic Zeolites. *Angew. Chem., Int. Ed.* **2006**, *45* (10), 1617−1620.
(47) Eyring, H. The Activated Complex in Chemical Reactions. *J. Chem. Phys.* **1935**, *3* (2), 107−115.
(48) Evans, M. G.; Polanyi, M. Some Applications of the Transition State Method to the Calculation of Reaction Velocities, Especially in Solution. *Trans. Faraday Soc.* **1935**, *31* (0), 875−894.
(49) Jones, A. J.; Iglesia, E. The Strength of Brønsted Acid Sites in Microporous Aluminosilicates. *ACS Catal.* **2015**, *5* (10), 5741−5755.
(50) Al-Nahari, S.; Dib, E.; Cammarano, C.; Saint-Germes, E.; Massiot, D.; Sarou-Kanian, V.; Alonso, B. Impact of Mineralizing Agents on Aluminum Distribution and Acidity of ZSM-5 Zeolites. *Angew. Chem., Int. Ed.* **2023**, *62* (7), No. e202217992.
(51) Han, O. H.; Kim, C.-S.; Hong, S. B. Direct Evidence for the Nonrandom Nature of Al Substitution in Zeolite ZSM-5: An Investigation by 27Al MAS and MQ MAS NMR. *Angew. Chem., Int. Ed.* **2002**, *41* (3), 469−472.
(52) Sklenak, S.; Dědeček, J.; Li, C.; Wichterlová, B.; Gábová, V.; Sierka, M.; Sauer, J. Aluminium Siting in the ZSM-5 Framework by Combination of High Resolution 27Al NMR and DFT/MM Calculations. *Phys. Chem. Chem. Phys.* **2009**, *11* (8), 1237−1247.
(53) Berkson, Z. J.; Hsieh, M.-F.; Smeets, S.; Gajan, D.; Lund, A.; Lesage, A.; Xie, D.; Zones, S. I.; McCusker, L. B.; Baerlocher, C.; Chmelka, B. F. Preferential Siting of Aluminum Heteroatoms in the Zeolite Catalyst Al-SSZ-70. *Angew. Chem., Int. Ed.* **2019**, *58* (19), 6255−6259.
(54) Lei, C.; Erlebach, A.; Brivio, F.; Grajciar, L.; Tošner, Z.; Heard, C. J.; Nachtigall, P. The Need for Operando Modelling of 27Al NMR in Zeolites: The Effect of Temperature, Topology and Water. *Chem. Sci.* **2023**, *14* (34), 9101−9113.
(55) Gómez-Hortigüela, L.; Pinar, A. B.; Corà, F.; Pérez-Pariente, J. Dopant-Siting Selectivity in Nanoporous Catalysts: Control of Proton Accessibility in Zeolite Catalysts through the Rational Use of Templates. *Chem. Commun.* **2010**, *46* (12), 2073−2075.
(56) Román-Leshkov, Y.; Moliner, M.; Davis, M. E. Impact of Controlling the Site Distribution of Al Atoms on Catalytic Properties in Ferrierite-Type Zeolites. *J. Phys. Chem. C* **2011**, *115* (4), 1096−1102.
(57) Tang, X.; Chen, W.; Dong, W.; Liu, Z.; Yuan, J.; Xia, H.; Yi, X.; Zheng, A. Framework Aluminum Distribution in ZSM-5 Zeolite Directed by Organic Structure-Directing Agents: A Theoretical Investigation. *Catal. Today* **2022**, *405*−*406*, 101−110.
(58) Zanardi, S.; Alberti, A.; Millini, R.; Bellussi, G.; Perego, G. Structural Characterization of Borosilicates Synthesized in the Presence of Ethylenediamine. In *Studies in Surface Science and Catalysis*; Aiello, R., Giordano, G., Testa, F., Eds.; Impact of Zeolites and other Porous Materials on the new Technologies at the Beginning of the New Millennium; Elsevier, 2002; Vol. *142*, pp 1923−1930.
(59) Perego, G.; Bellussi, G.; Millini, R.; Alberti, A.; Zanardi, S. B-Containing Molecular Sieves Crystallized in the Presence of Ethylenediamine. Part II: Crystal Structure of as-Synthesized B-MFI. *Microporous Mesoporous Mater.* **2003**, *58* (3), 213−223.
(60) First, E. L.; Gounaris, C. E.; Wei, J.; Floudas, C. A. Computational Characterization of Zeolite Porous Networks: An Automated Approach. *Phys. Chem. Chem. Phys.* **2011**, *13* (38), 17339−17358.
(61) Balcom, H.; Hoffman, A. J.; Locht, H.; Hibbitts, D. Brønsted Acid Strength Does Not Change for Bulk and External Sites of MFI Except for Al Substitution Where Silanol Groups Form. *ACS Catal.* **2023**, *13* (7), 4470−4487.
(62) Derouane, E. G. Shape Selectivity in Catalysis by Zeolites: The Nest Effect. *J. Catal.* **1986**, *100* (2), 541−544.
(63) Van der Mynsbrugge, J.; De Ridder, J.; Hemelsoet, K.; Waroquier, M.; Van Speybroeck, V. Enthalpy and Entropy Barriers Explain the Effects of Topology on the Kinetics of Zeolite-Catalyzed Reactions. *Chem.—Eur. J.* **2013**, *19* (35), 11568−11576.
(64) Wang, S.; Iglesia, E. Catalytic Diversity Conferred by Confinement of Protons within Porous Aluminosilicates in Prins Condensation Reactions. *J. Catal.* **2017**, *352*, 415−435.
(65) Sarazen, M. L.; Iglesia, E. Experimental and Theoretical Assessment of the Mechanism of Hydrogen Transfer in Alkane-Alkene Coupling on Solid Acids. *J. Catal.* **2017**, *354*, 287−298.
(66) Herrmann, S.; Iglesia, E. Selective Conversion of Acetone to Isobutene and Acetic Acid on Aluminosilicates: Kinetic Coupling between Acid-Catalyzed and Radical-Mediated Pathways. *J. Catal.* **2018**, *360*, 66−80.
(67) Veefkind, V. A.; Smidt, M. L.; Lercher, J. A. On the role of strength and location of Brønsted acid sites for ethylamine synthesis on mordenite catalysts. *Appl. Catal., A* **2000**, *194*−*195*, 319−332.
(68) Bhan, A.; Allian, A. D.; Sunley, G. J.; Law, D. J.; Iglesia, E. Specificity of Sites within Eight-Membered Ring Zeolite Channels for Carbonylation of Methyls to Acetyls. *J. Am. Chem. Soc.* **2007**, *129* (16), 4919−4924.
(69) Zones, S. I.; Chen, C. Y.; Benin, A.; Hwang, S.-J. Opportunities for Selective Catalysis within Discrete Portions of Zeolites: The Case for SSZ-57LP. *J. Catal.* **2013**, *308*, 213−225.

https://doi.org/10.1021/jacs.4c00373
J. Am. Chem. Soc. 2024, 146, 10666−10678